

EVOLUTION OF OH AND CO-DARK MOLECULAR GAS FRACTION ACROSS A MOLECULAR CLOUD BOUNDARY IN TAURUS

DUO XU^{1,2*}, DI LI^{1,3*}, NANNAN YUE^{1,2}, PAUL F. GOLDSMITH⁴¹ National Astronomical Observatories, Chinese Academy of Sciences, A20 Datun Road, Chaoyang District, Beijing 100012, China² University of Chinese Academy of Sciences, Beijing 100049, China³ Key Laboratory for Radio Astronomy, Chinese Academy of Sciences⁴ Jet Propulsion Laboratory, California Institute of Technology, Pasadena, CA 91109, USA

ABSTRACT

We present observations of ¹²CO J=1-0, ¹³CO J=1-0, H_I, and all four ground-state transitions of the hydroxyl (OH) radical toward a sharp boundary region of the Taurus molecular cloud. Based on a PDR model that reproduces CO and [C_I] emission from the same region, we modeled the three OH transitions, 1612, 1665, 1667 MHz successfully through escape probability non-LTE radiative transfer model calculations. We could not reproduce the 1720 MHz observations, due to un-modeled pumping mechanisms, of which the most likely candidate is a C-shock. The abundance of OH and CO-dark molecular gas (DMG) are well constrained. The OH abundance [OH]/[H₂] decreases from 8×10^{-7} to 1×10^{-7} as A_v increases from 0.4 to 2.7 mag, following an empirical law

$$[\text{OH}]/[\text{H}_2] = 1.5 \times 10^{-7} + 9.0 \times 10^{-7} \times \exp(-A_v/0.81),$$

which is higher than PDR model predictions for low extinction regions by a factor of 80. The over-abundance of OH at extinctions at or below 1 mag is likely the result of a C-shock. The dark gas fraction (DGF, defined as fraction of molecular gas without detectable CO emission) decreases from 80% to 20%, following a gaussian profile

$$\text{DGF} = 0.90 \times \exp\left(-\left(\frac{A_v - 0.79}{0.71}\right)^2\right).$$

This trend of the DGF is consistent with our understanding that the DGF drops at low visual extinction due to photodissociation of H₂ and drops at high visual extinction due to CO formation. The DGF peaks in the extinction range where H₂ has already formed and achieved self-shielding but ¹²CO has not. Two narrow velocity components with a peak-to-peak spacing of $\sim 1 \text{ km s}^{-1}$ were clearly identified. Their relative intensity and variation in space and frequency suggest colliding streams or gas flows at the boundary region.

Subject headings: ISM: clouds – ISM: individual objects (Taurus) – ISM: molecules – ISM: evolution

1. INTRODUCTION

The formation of molecular hydrogen is a critical step in the transformation of interstellar gas into new stars. Various complex processes in the transformation between atomic gas and molecular gas result in changes of the physical state of gas. These changes affect the star formation process in galaxies, and thus their evolution. It is of great significance to study the physical conditions in regions where the transformation between atomic gases and molecular gases occurs. The boundaries of molecular clouds are locations where the chemical composition changes considerably and primarily atomic gas transforms into molecular gas.

Apart from traditional tracers such as CO and H_I, the hydroxyl radical, OH, is thought to be an excellent tracer to determine the physical conditions of the early state ISM, where CO is absent (Li et al. 2015). Such early state molecular ISM appears in boundary regions. A three-way comparison of H_I, OH and CO lines is expected to show molecular features in OH which are not traced by CO, but which highlight the transition from atomic gas (seen in the H_I line) to molecular gas.

Additionally, OH can be the tracer of “J-shocks”

(Medling et al. 2015) and “C-shocks” (Anderl et al. 2013). Shock waves play a major role in the ISM (Timmermann 1998). When shock waves propagate through the molecular ISM the ambient gas is compressed, heated, and accelerated. Furthermore, the composition of the gas is significantly changed when chemical reactions occur especially in the warm shocked gas located in outermost parts of the transition region. The abundance of OH can vary from 10^{-5} to 10^{-11} when a 10 km s^{-1} C-type shock propagates into a diffuse cloud with $n_{\text{H}} = 50 \text{ cm}^{-3}$ (Draine & Katz 1986). Thus, searching for the evidence of shocks at the boundary region via OH lines is of great significance.

The boundary of molecular clouds is the region where all the physical and chemical processes mentioned above take place. As the dramatic changes of species at the boundaries, the physical conditions at the boundaries are distinct from those in other places. A clear example of cloud boundaries can be found in Taurus (Goldsmith et al. 2008) north east of the TMC1 region. Orr et al. (2014) compared the observations of Taurus boundaries with line intensities produced by the Meudon PDR code. They found a low ratio of ¹²C to ¹³C ~ 43 , and a highly depleted sulfur abundance (by a factor ≥ 50) to explain the very low [C_I] emission. Moreover, Goldsmith et al.

*Email: xuduo117@nao.cas.cn, dili@nao.cas.cn

(2010) found an unexpectedly high degree of excitation of the H_2 in the boundary layer of Taurus molecular cloud. They believed that an enhanced heating rate may be the result of turbulent dissipation.

As we are interested in the changes of chemical composition across the boundaries to study the transition between atomic- and molecular-dominated gas, we need to find a boundary of molecular clouds without significant UV enhancement. H_2 can be destroyed by UV photons, making the statistical equilibrium function complex. Moreover, it is easier to detect the emission of molecular tracers such as OH without an enhanced UV field. We thus observed the Taurus boundary studied by Goldsmith et al. (2010) and Orr et al. (2014), which has a relatively low UV field between $\chi=0.3$ and 0.8 in units of the Draine's field (Flagey et al. 2009; Pineda et al. 2010) and little foreground or background visual extinction (Padoan et al. 2002), making it favorable for the comparison of observations with physical models.

We have carried out observations of the Taurus boundary in four OH transitions (1612, 1665, 1667, and 1720 MHz) using the 305 m Arecibo Telescope. We made a total of five cuts across the boundary region each with 17 pointings 3 arcminute apart (Fig. 1). We describe the observations of OH across the boundary region, and the H I , ^{12}CO J=1-0, and ^{13}CO J=1-0 map of Taurus molecular cloud in Section 2. We analyze the OH spectrum and derive the physical parameters of ^{13}CO across the boundary in Section 3. We use a cylindrical model and RADEX to fit OH lines to determine the physical parameters in Section 4. We discuss the conjugate emission of OH and pumping mechanisms in Section 5. In Section 6, we summarize our results and conclusions from this study.

2. OBSERVATIONS AND DATA

We carried out observations of OH with the Arecibo Telescope in Project a2813. We extracted H I data from the GALFA- H I survey, and extracted ^{12}CO J=1-0 and ^{13}CO J=1-0 data from the FCRAO Taurus survey.

2.1. OH Observations

The OH observations were taken using the L-band wide receiver (with frequency range 1.55-1.82 GHz) on October 28-31, 2013. We observed four OH transition lines at the rest frequencies of 1612.231, 1665.402, 1667.359, and 1720.530 MHz with the total power ON mode. Spectra were obtained with the Arecibo WAPP correlator with nine-level sampling and 4096 spectral channels for each line in each polarization. The spectral bandwidth was 3.13 MHz for a channel spacing of about 763 Hz, or 0.142 km s^{-1} . The average system temperature was about 31 K. The main beam of the antenna pattern had a full-width at half-maximum (FWHM) beam-width of $3'$. Spectra were taken at 17×5 positions across the Taurus boundary region (TBR), as seen in Fig. 1. An integration time of 300 seconds per position was used resulting in an RMS noise level of about 0.027 K.

2.2. H I Data

H I 21 cm observations of the Taurus boundary region were extracted from the results of the Galactic Arecibo L-Band Feed Array H I (GALFA- H I) survey (Peek et

al. 2011). GALFA- H I uses ALFA, a seven-beam array of receivers mounted at the focal plane of the 305 m Arecibo telescope, to map H I emission in the Galaxy. GALFA- H I is a survey of the Galactic interstellar medium in the 21 cm line hyperfine transition of neutral hydrogen which covers a large-area ($13,000 \text{ deg}^2$) with $\sim 4'$ resolution, and has high spectral resolution (0.18 km s^{-1}) with broad velocity coverage ($-700 \text{ km s}^{-1} < v_{\text{LSR}} < +700 \text{ km s}^{-1}$). Typical RMS noise is 80 mK in a 1 km s^{-1} channel.

2.3. ^{12}CO and ^{13}CO Data

The ^{12}CO J=1-0 and ^{13}CO J=1-0 observations were taken simultaneously between 2003 and 2005 using the 13.7 m Five College Radio Astronomy Observatory (FCRAO) Telescope (Narayanan et al. 2008). The map is centered at $\alpha(2000.0) = 04^{\text{h}}32^{\text{m}}44.6^{\text{s}}$, $\delta(2000.0) = 24^{\circ}25'13.08''$, with an area of $\sim 98 \text{ deg}^2$. The main beam of the antenna pattern had a full-width to half-maximum (FWHM) beam-width of $45''$ for ^{12}CO , and $47''$ for ^{13}CO . The angular spacing (pixel size) of the resampled on the fly (OTF) data is $20''$ (Goldsmith et al. 2008), which corresponds to a physical scale of $\approx 0.014 \text{ pc}$ at a distance of $D = 140 \text{ pc}$. The data have a mean rms antenna temperature of 0.28 K and 0.125 K, in channels of 0.26 km s^{-1} and 0.27 km s^{-1} width for ^{12}CO and ^{13}CO , respectively.

3. ANALYSIS

3.1. Spectral Analysis

The locations of the positions for the telescope pointing used to study the TBR are shown in Fig. 1. To examine the transition zone with higher signal to noise ratio, we averaged all five cuts of spectra of OH 1612 MHz, 1665 MHz, 1667 MHz, 1720 MHz, ^{12}CO J=1-0, ^{13}CO J=1-0, and H I , as shown in Fig. 2. The ^{12}CO J=1-0 and ^{13}CO J=1-0 spectra were convolved to the OH beam size of $3'$ at each position. The emission lines of OH, ^{12}CO J=1-0, ^{13}CO J=1-0, and the absorption lines of H I are well matched in velocity. Especially, the emission lines of OH 1665 MHz at positions 10 to 12 all have two components, and the spectral of H I at the same point have two corresponding narrow absorption components, as shown in Fig. 3.

We did gaussian fitting of the OH 1612 MHz, 1665 MHz, 1667 MHz, 1720 MHz spectral with two gaussian components, the fitting of ^{12}CO and ^{13}CO spectra with a single gaussian component, and the fitting of H I spectra with three gaussian components. We show the spectra and the fitted profiles in Fig. 2. The line ratio between OH 1665 MHz and 1667 MHz is greater than 1 in the outside TBR region (TBR-O) as shown in Fig. 2. Under the assumption of LTE, the line ratio between 1665 MHz and 1667 MHz ranges from 0.6 to 1. The line ratio greater than 1 indicates a deviation from LTE for OH.

We show the change of peak intensity of two components in OH 1665 MHz and a single component in ^{13}CO across the TBR in Fig. 4. Component 1 of OH 1665 MHz spectrum at 5.3 km s^{-1} appears after position 4, and gets stronger across the TBR. Component 2 at 6.8 km s^{-1} appears in the TBR-O and gets faint in the inside TBR region (TBR-I), and disappears after position 13. The central velocities of ^{13}CO shift from 6.3 km s^{-1} to 5.7 km s^{-1} . We assume that each component of the OH emission indicates a gas stream. When the intensity

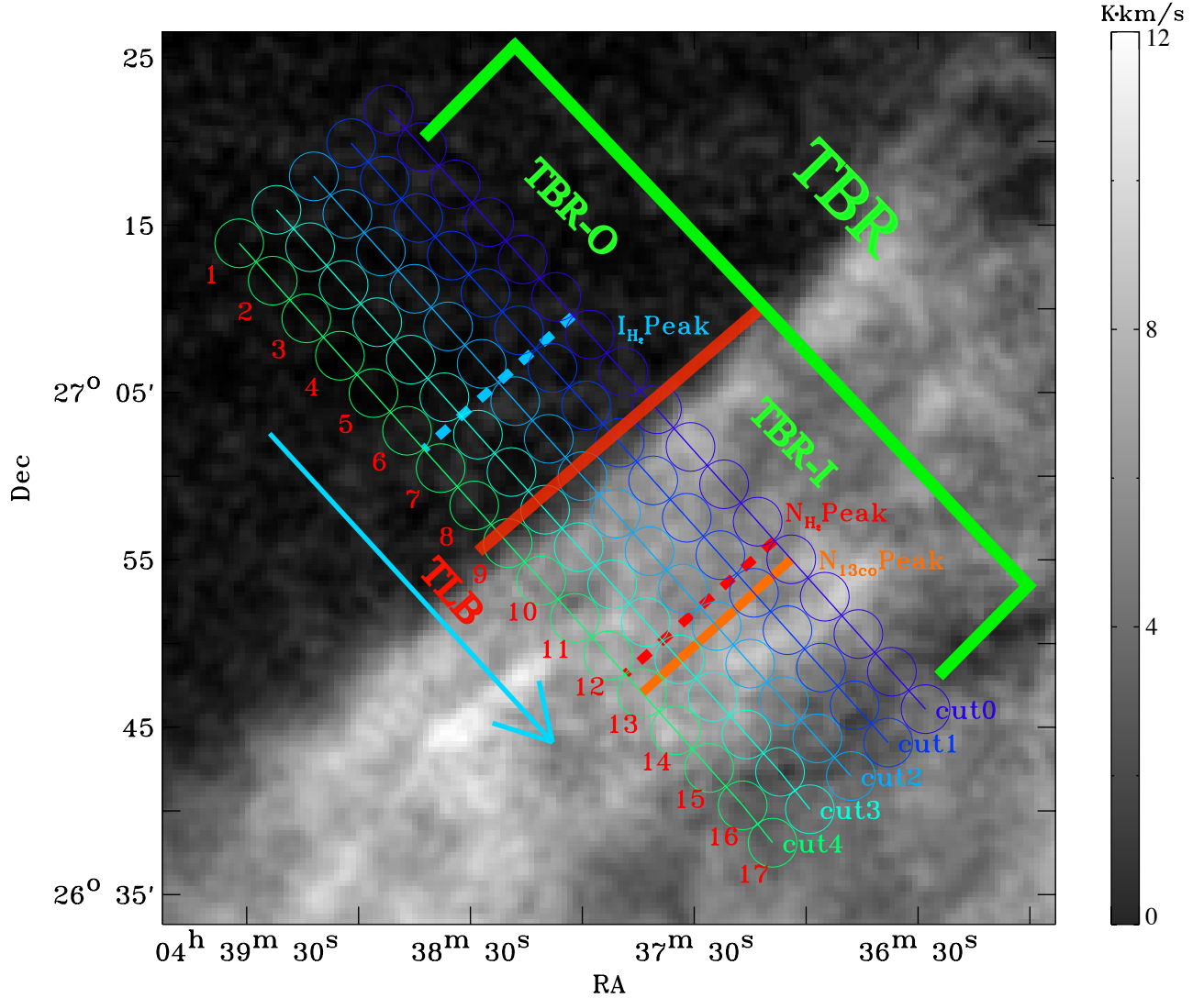


FIG. 1.— The boundary region in ^{13}CO $J=1-0$ peak intensity, with observed positions indicated. The size of circle indicates the OH beam size $\sim 3'$. The numbers of positions are shown in the figure. The whole region is Taurus boundary region and is denoted TBR. The Taurus linear boundary (TLB) located at position 9 is shown as red line. The outside and inside region of the TBR are abbreviated as TBR-O and TBR-I respectively. The peak intensity of two lowest rotational transitions of H_2 , $\text{S}(0)$ and $\text{S}(1)$, is located between position 6 and position 7 (Goldsmith et al. 2010). The peak column density of H_2 is located between position 12 and position 13. The peak column density of ^{13}CO is located at position 13. The arrow in the figure indicates the direction we present spectral line maps.

of OH component 2 is stronger than that of component 1 in TBR-O, the central velocity of ^{13}CO is located at 6.3 km s^{-1} . When the intensity of OH component 1 is stronger than that of component 2 in TBR-I, the central velocity of ^{13}CO is located at 5.7 km s^{-1} . The central velocity of ^{13}CO shifts in the same way as the central velocity of stronger intensity OH component shifts. From Fig. 3 we see that component 2 of OH 1665 gradually becomes fainter, and disappears at position 13. At the same time the central velocity of component 1 gradually shifts from 5.3 km s^{-1} at position 9 to 5.8 km s^{-1} at position 13, which indicates that the collision of two streams results in the final central velocity being located between the velocities of the two components. The central velocity of the final combined stream is located closer to component 1, which has a stronger emission line in TBR-I. This is consistent with the assumption of differ-

ent amounts of ^{13}CO emission at different velocities. Not only OH 1665 MHz but also ^{13}CO shows the central velocity shifting after the streams collide from position 10 to position 13 in Fig. 3.

We show the change of line width along the cut direction in Fig. 5. We can clearly see that the line width of ^{12}CO and ^{13}CO peak at the TLB. This mainly due to the two gas streams which contribute to the line width of ^{12}CO and ^{13}CO . The line width of OH 1667 MHz is much wider than that of other lines in TBR-O. This is mainly caused by the weak emission lines of OH 1667 MHz in TBR-O. Since the height of OH 1667 MHz is small in TBR-O, the fitted gaussian profile tends to be flatter than that at other positions. So the line width of OH 1667 MHz is two times wider than that of the other three lines in TBR-O. Component 2 of OH 1667 MHz whose central velocity is at 6.8 km s^{-1} is very weak in

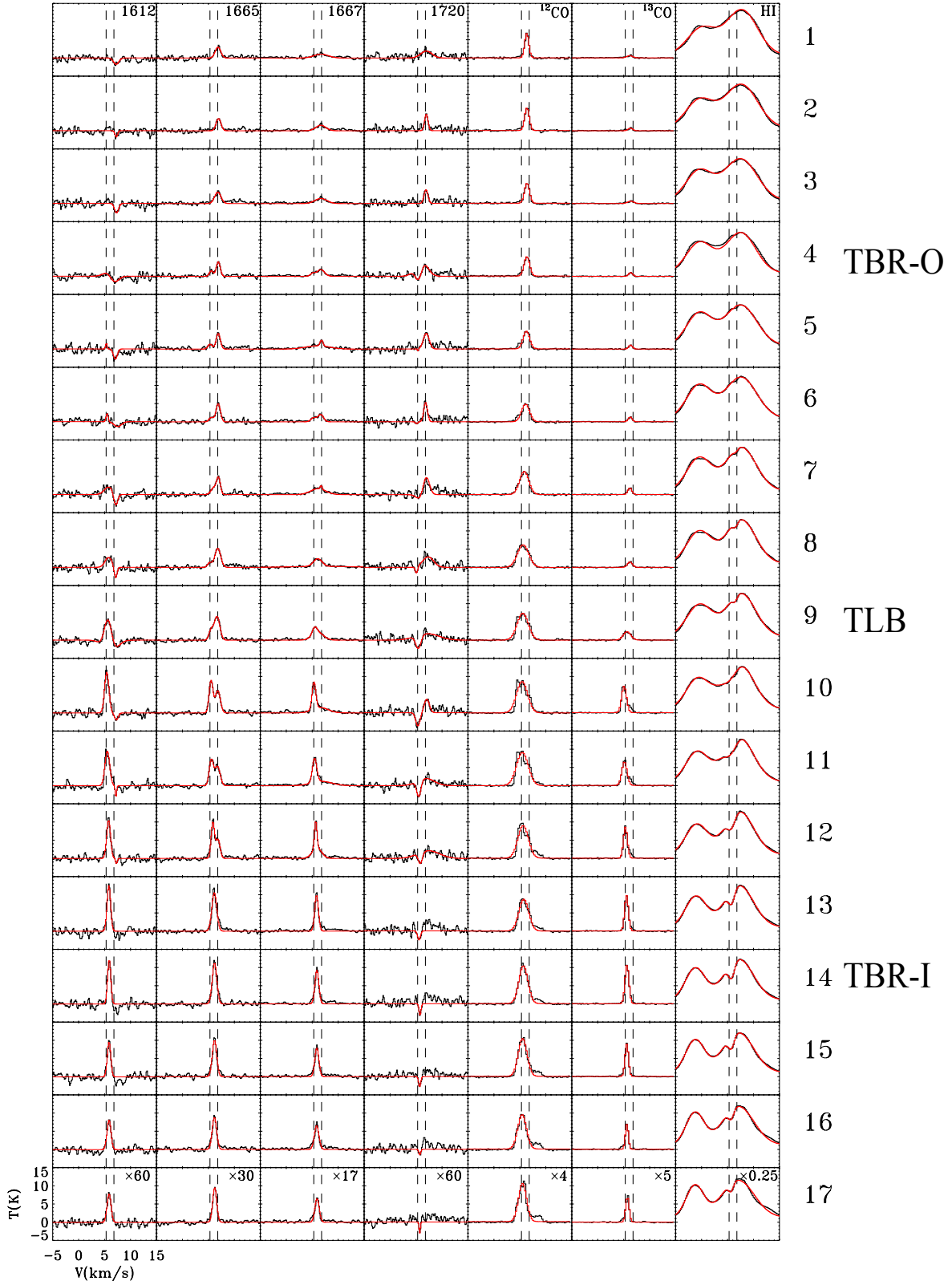


FIG. 2.— Average spectra of all five cuts of OH 1612 MHz, 1665 MHz, 1667 MHz, 1720 MHz, ^{12}CO J=1-0, ^{13}CO J=1-0, and HI overlaid with corresponding fitted gaussian profile (red curve). The ^{12}CO J=1-0 and ^{13}CO J=1-0 spectra were convolved to the OH beam size of $3''$ at each position. We fitted the OH 1612 MHz, 1665 MHz, 1667 MHz, 1720 MHz spectra with two gaussian components, fitted the ^{12}CO J=1-0 and ^{13}CO J=1-0 spectra with single gaussian component, and fitted the HI spectra with three gaussian components. The vertical dashed lines indicate the central velocities of the two components of OH 1665 MHz at position 10.

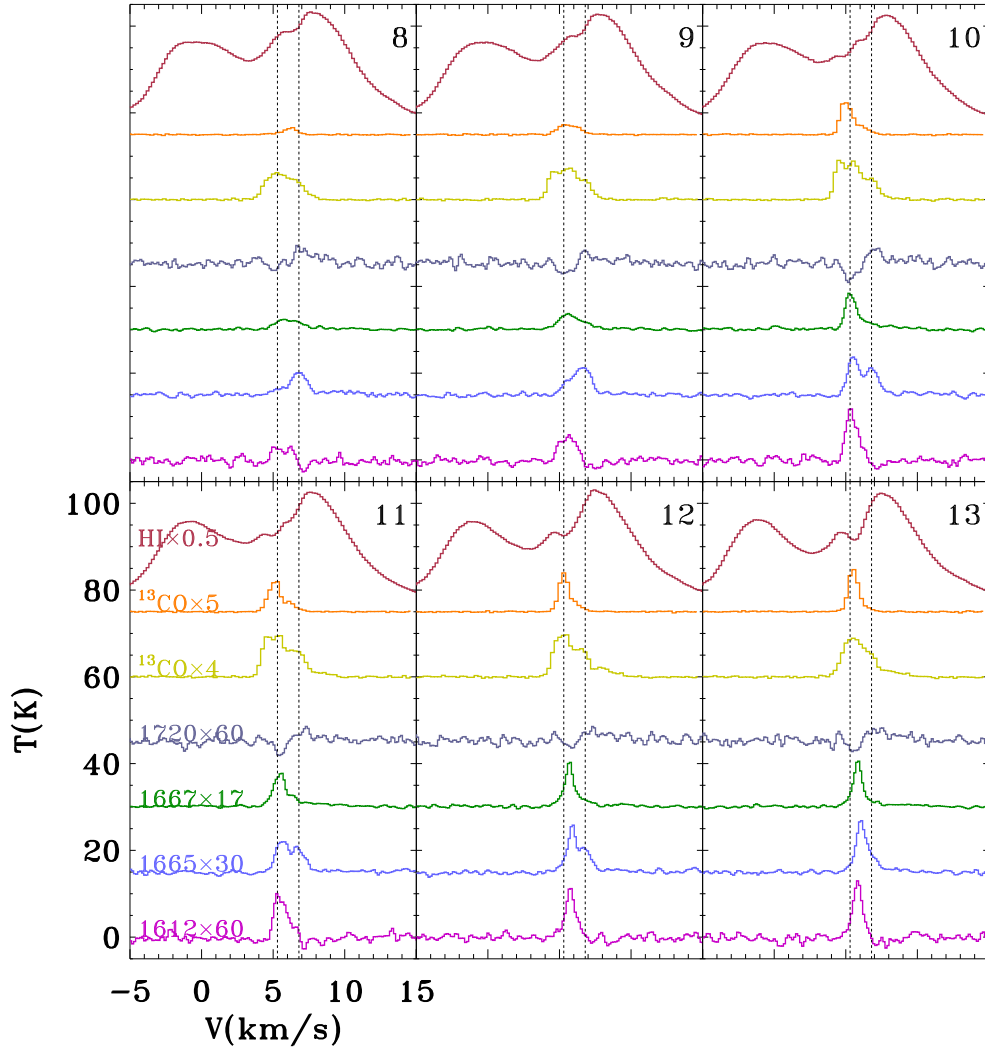


FIG. 3.— Average spectra of all five cuts of OH 1612 MHz, 1665 MHz, 1667 MHz, 1720 MHz, ^{12}CO J=1-0, ^{13}CO J=1-0, and HI at positions 8 to 13. The ^{12}CO J=1-0 and ^{13}CO J=1-0 spectra were convolved to the OH beam size of $3'$ at each position. The vertical dashed lines indicate the central velocities of the two components of OH 1665 MHz at position 10.

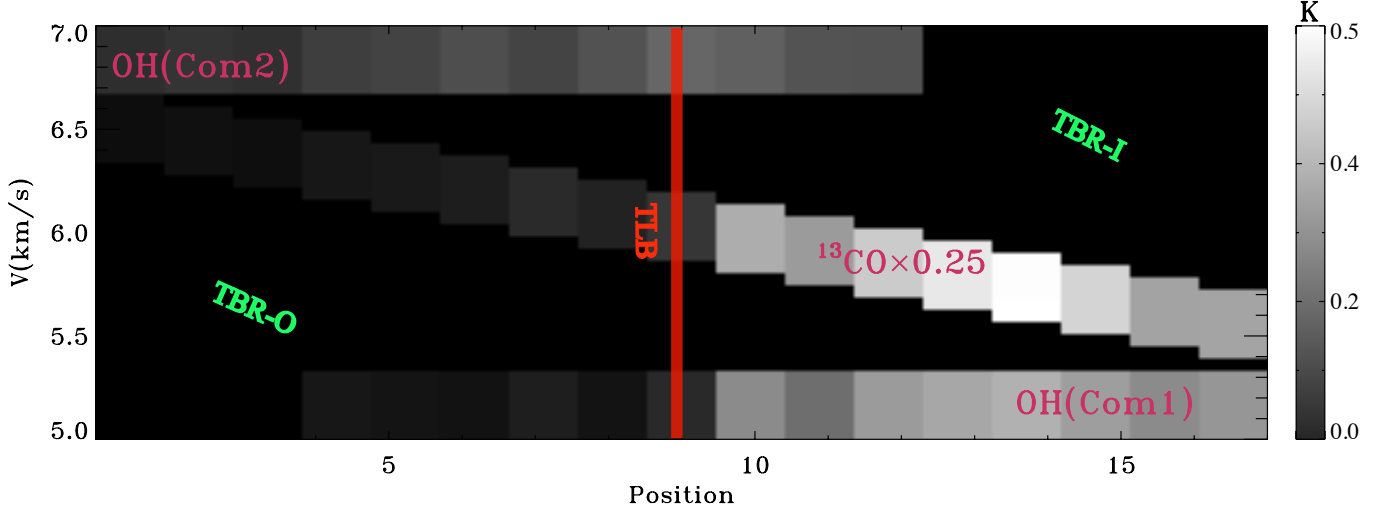


FIG. 4.— Change of peak intensity of the two components of OH 1665 and the single component of ^{13}CO across the TBR. The upper stripe indicates the intensity of component 2 in OH 1665 MHz across the TBR. The middle oblique stripe indicates the intensity of ^{13}CO . The bottom stripe indicates the intensity of component 1 in OH 1665 MHz across the TBR. The color indicates the value of peak intensity of each spectrum at each position. The peak intensity of ^{13}CO shown in the oblique stripe is one fourth of the observed peak intensity. A more detailed discussion is in Section 3.1.

some positions in TBR-I, which leads to a wider line wing of the component 1, as shown in Fig. 2. The width of component 2 in TBR-I is wider than that of other three lines in TBR-I, which leads to the average line width of OH 1667 behaving in an erratic way. The line width of OH 1665 MHz is nearly constant across the TBR.

The line width of ^{12}CO is significantly greater than that of ^{13}CO . Opacity may be one of the reasons. Owing to the different abundance of ^{12}CO and ^{13}CO , τ_{12} is almost 70 times larger than τ_{13} . When τ_{12} is much larger than unity, the term $1 - \exp[-\tau_{12}\phi(\Delta\mathbf{v})]$ in the line profile of ^{12}CO is much wider than that of ^{13}CO , where $\phi(\Delta\mathbf{v})$ is a gaussian profile of the velocity offset from line center $\Delta\mathbf{v}$. We made an estimate of the line width ratio between ^{12}CO and ^{13}CO only considering the opacity. In TBR-O, the optical depth range from 0.05 to 0.4. We took position 8 having $\tau_{13\text{CO}} = 0.2$ as an example. The line width ratio between ^{12}CO and ^{13}CO is 1.4, which is much less than the observed ratio 2.3. Other broadening mechanisms must occur in the TBR. Park & Hong (1995) took different broadening mechanisms such as micro-turbulence and macro-turbulence into consideration and found that the line width ratio between ^{12}CO and ^{13}CO can range from 1 to 3 depending on the physical condition of the gas, which just corresponds to the line width ratio between ^{12}CO and ^{13}CO in our work. The wider line width of ^{12}CO may be the result of larger turbulence due to the more extended distribution of ^{12}CO . According to Larson's law (Larson 1981), a larger scale of a molecular cloud leads to a larger velocity dispersion. Considering current geometrical model of photo-dissociation region (Tielens 2005), the larger self-shielding threshold of ^{13}CO makes it more constrained to the inner region of the boundary, which yields a narrower line width than that of ^{12}CO .

We can also see the central velocities of component 1 in OH 1665 MHz shifting from 5.3 km s^{-1} to 6.0 km s^{-1} at positions 10-12 in Fig. 3. This velocity gradient may be caused by colliding streams or gas flow at the TLB. The

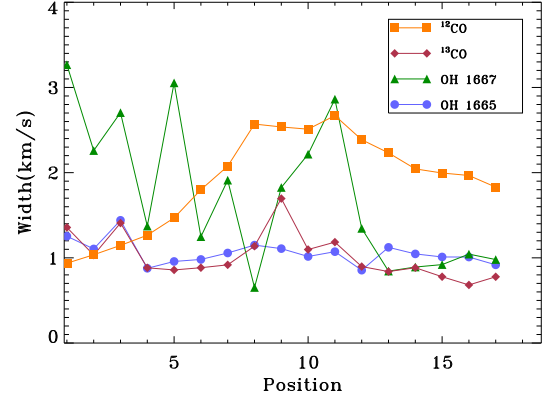


FIG. 5.— The change of line width of OH 1665 MHz, 1667 MHz, ^{12}CO J=1-0 and ^{13}CO J=1-0 along the cut direction shown in Fig. 1.

description of the OH spectra and components across TBR can be found in Table 1.

3.2. ^{13}CO Column Density Calculation

From the fitting result of ^{12}CO J=1-0 and ^{13}CO J=1-0 above, we can calculate the column density of ^{13}CO . The column density of ^{13}CO in the upper-level ($J = 1$) can be written as

$$N_{u,^{13}\text{CO}} = \frac{8\pi k\nu^2}{hc^3 A_{ul}} \int T_b(V) dV, \quad (1)$$

where k is Boltzmann's constant, h is Planck's constant, c is the speed of light, A_{ul} is the spontaneous decay rate from the upper level to the lower level, and T_b is the brightness temperature. A convenient form of this equation is

$$\left(\frac{N_{u,^{13}\text{CO}}}{\text{cm}^{-2}} \right) = 3.6 \times 10^{14} \int \left(\frac{T_b}{\text{K}} \right) d \left(\frac{V}{\text{km s}^{-1}} \right). \quad (2)$$

TABLE 1
THE CHANGE OF OH SPECTRAL LINES ACROSS THE BOUNDARY IN TAURUS

Position	Offset	OH spectral lines							
ID	(')	1612 MHz		1665 MHz	1667 MHz				1720 MHz
		$\mathfrak{C}1^1$	$\mathfrak{C}2^2$	$\mathfrak{C}1$	$\mathfrak{C}2$	$\mathfrak{C}1$	$\mathfrak{C}2$	$\mathfrak{C}1$	$\mathfrak{C}2$
1 (outer)	-24.0	$w\mathfrak{e}^{*3}$	\mathfrak{a}^6	\mathfrak{n}	\mathfrak{e}	\mathfrak{n}	$w\mathfrak{e}$	\mathfrak{n}	$w\mathfrak{e}$
7 (I_{H_2} peak)	-6.0	$w\mathfrak{e}$	\mathfrak{a}	\mathfrak{n}	\mathfrak{e}	$w\mathfrak{e}$	$w\mathfrak{e}$	\mathfrak{n}	\mathfrak{e}
9 (boundary)	0.0	\mathfrak{e}^4	$w\mathfrak{a}^7$	\mathfrak{e}	\mathfrak{e}	\mathfrak{e}	$w\mathfrak{e}$	\mathfrak{a}	\mathfrak{e}
11 (N_{H_2} peak)	6.0	$\mathfrak{e}(\rightarrow^5)$	\mathfrak{n}^8	$\mathfrak{e}(\rightarrow)$	\mathfrak{e}	$\mathfrak{e}(\rightarrow)$	$w\mathfrak{e}$	$\mathfrak{a}(\rightarrow)$	$w\mathfrak{e}$
12 (N_{CO} peak)	9.0	$\mathfrak{e}(\rightarrow)$	\mathfrak{n}	$\mathfrak{e}(\rightarrow)$	$w\mathfrak{e}$	$\mathfrak{e}(\rightarrow)$	\mathfrak{n}	$\mathfrak{a}(\rightarrow)$	\mathfrak{n}
17 (inner)	24.0	$\mathfrak{e}(\rightarrow)$	\mathfrak{n}	$\mathfrak{e}(\rightarrow)$	\mathfrak{n}	$\mathfrak{e}(\rightarrow)$	\mathfrak{n}	$\mathfrak{a}(\rightarrow)$	\mathfrak{n}

¹ $\mathfrak{C}1$ means the component at 5.3 km s⁻¹.

² $\mathfrak{C}2$ means the component at 6.8 km s⁻¹.

³ $w\mathfrak{e}$ means weak emission.

⁴ \mathfrak{e} means emission.

⁵ \rightarrow means the shifting of central velocity of component 1.

⁶ \mathfrak{a} means absorption.

⁷ $w\mathfrak{a}$ means weak absorption.

⁸ \mathfrak{n} means neither emission nor absorption.

The total ^{13}CO column density N_{tot} is related to the upper level column density N_u through (Li 2002)

$$N_{\text{tot},^{13}\text{CO}} = f_u f_\tau f_b N_{u,^{13}\text{CO}}. \quad (3)$$

In the equation above, the level correction factor f_u can be calculated analytically under the assumption of local thermal equilibrium (LTE) as

$$f_u = \frac{Q(T_{\text{ex}})}{g_u \exp\left(-\frac{h\nu}{kT_{\text{ex}}}\right)}, \quad (4)$$

where g_u is the statistical weight of the upper-level. T_{ex} is the excitation temperature and $Q(T_{\text{ex}}) = kT_{\text{ex}}/hB_0$ is the LTE partition function, where B_0 is the rotational constant (Tennyson 2005). A convenient form of the LTE partition function is $Q(T_{\text{ex}}) \approx T_{\text{ex}}/2.76\text{K}$. The correction factor for opacity is defined as

$$f_\tau = \frac{\int \tau_{13} dv}{\int (1 - e^{-\tau_{13}}) dv}, \quad (5)$$

and the correction for the background

$$f_b = \left[1 - \frac{e^{\frac{h\nu}{kT_{\text{ex}}}} - 1}{e^{\frac{h\nu}{kT_{\text{bg}}}} - 1}\right]^{-1}, \quad (6)$$

where τ_{13} is the opacity of the ^{13}CO transition and T_{bg} is the background temperature, assumed to be 2.7K.

The ^{13}CO opacity is estimated as follows. Assuming equal excitation temperatures for the two isotopologues, the ratio of the brightness temperature of ^{12}CO to that of ^{13}CO can be written as

$$\frac{T_{b,12}}{T_{b,13}} = \frac{1 - e^{-\tau_{12}}}{1 - e^{-\tau_{13}}}. \quad (7)$$

Assuming $\tau_{12} \gg 1$, the opacity of ^{13}CO can be written as

$$\tau_{13} = -\ln\left(1 - \frac{T_{b,13}}{T_{b,12}}\right). \quad (8)$$

The excitation temperature T_{ex} is obtained from the ^{12}CO intensity. First, the maximum intensity in the spectrum of each pixel is found. This quantity is denoted by T_{max} . The excitation temperature is calculated

by solving the following equation

$$T_{\text{max}} = \frac{h\nu}{k} \left[\frac{1}{e^{\frac{h\nu}{kT_{\text{ex}}}} - 1} - \frac{1}{e^{\frac{h\nu}{kT_{\text{bg}}}} - 1} \right], \quad (9)$$

where h , k and ν are Planck's constant, Boltzmann's constant, and the central frequency of ^{12}CO $J = 1 \rightarrow 0$ line (115.27 GHz), respectively.

To examine the LTE assumption when calculating the physical parameters of CO, we used a spherical 1-d non-LTE spectral analysis radiative transfer model, RADEX (van der Tak et al. 2007) to derive the excitation temperature of ^{12}CO and ^{13}CO . We took position 10 as an example. We assumed the number density of H_2 to be 400 cm⁻³, which is given by Orr et al. (2014). We also assumed the kinetic temperature to be 15 K, which is widely applied in the relatively diffuse region in the Taurus molecular cloud (e.g. Goldsmith et al. 2008). The resulting excitation temperature of ^{12}CO and ^{13}CO are $T_{\text{ex},^{12}\text{CO}} = 7.7\text{ K}$ and $T_{\text{ex},^{13}\text{CO}} = 6.8\text{ K}$, with a difference of about 10%. The assumption that the excitation temperatures of ^{12}CO and ^{13}CO are equal seems reasonable. Owing to the difference of excitation temperature between ^{12}CO and ^{13}CO , the derived column density of ^{13}CO also has an error about 10%.

We show the change of excitation temperature of ^{13}CO and the change of column density of ^{13}CO along the cut direction in Table 2 and Fig. 6. The excitation temperature T_{ex} of ^{13}CO increases crossing the boundary. The column density of ^{13}CO shows a peak at position 13 and 14 inside the boundary.

4. SIMULATION OF OH EMISSION LINE WITH RADEX

We assume a cylindrical geometry to model the linear boundary region of the cloud. We adopted the results of “cylindricalized” Meudon PDR model by Orr et al. (2014) and applied a spherical 1-d non-LTE spectra analysis radiative transfer model, RADEX (van der Tak et al. 2007), to generate a sky-plane image of the TBR for the transitions of OH.

4.1. Density Profile of Taurus Boundary Region

We modeled the linear boundary as a cylinder with a radius-dependent H_2 volume density structure of the

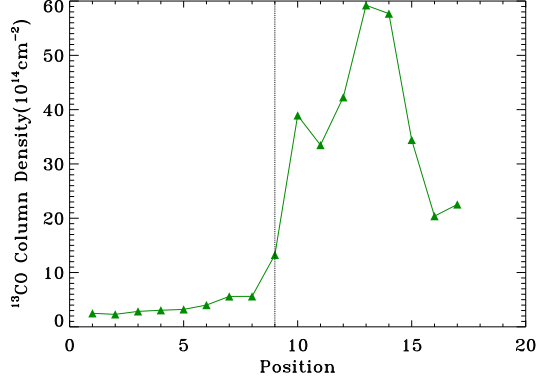


FIG. 6.— The change of column density of ^{13}CO along the cut direction.

TABLE 2
PARAMETERS ALONG THE BOUNDARY

position	$T_{\text{ex},^{13}\text{CO}}$ (K)	$N_{^{13}\text{CO}}$ (10^{14}cm^{-2})
1	6.5	2.5
2	6.3	2.3
3	5.9	2.8
4	5.8	3.1
5	5.6	3.2
6	5.6	4.0
7	6.3	5.6
8	6.3	5.6
9	6.9	13
10	7.6	39
11	7.8	33
12	7.7	42
13	7.6	59
14	8.5	58
15	8.5	34
16	8.0	20
17	8.5	23

following form (King 1962),

$$n_{\text{H}_2}(r) = \begin{cases} n_c a^2 / (r^2 + a^2) & : r \leq R \\ 0 & : r > R \end{cases} \quad (10)$$

This functional form was used in analysis of the Taurus region by Pineda et al. (2010).

This profile has a flat high-density center, which then transitions to a region of power-law decay, and finally, at a truncating radius, the density is set to zero. It assumes only three parameters, the central core density n_c , a parameter characterizing the width of the central core a , and the truncating radius R . Orr et al. (2014) fitted the profile with visual extinction data for this region. The fitted values for the density profile parameters are $n_c = 626 \text{ cm}^{-3}$, $a = 0.457 \text{ pc}$, and $R = 1.80 \text{ pc}$. The axis of the cylindrical distribution is centered $11.5'$ to the southwest of the boundary position between position 12 and position 13.

The H_2 volume density of 17 observed points along the boundary is obtained from Orr et al. (2014).

4.2. RADEX Fitting Results

RADEX takes the following inputs: kinetic temperature (T_k), density of H_2 (n_{H_2}), H_2 ortho-to-para ratio (OPR), background temperature (T_{bg}), column density of OH (N_{OH}), and line width (Δv_{OH}). Rates for collisional excitation of OH are taken from Offer et al. (1994).

The n_{H_2} is an input parameter estimated based on the cylindrical model in Orr et al. (2014). The Galactic background emission is estimated to be about 0.8 K by extrapolating the standard interstellar radiation field (ISRF) to L band (Winnberg et al. 1980). $T_{\text{bg}} = 3.5 \text{ K}$ is thus used in the simulation.

We vary the T_k , H_2 OPR and N_{OH} to find the optimum model by minimizing χ^2 for the four OH lines, defined as

$$\chi^2 = \frac{1}{N} \sum_{i=1}^N \frac{(I_{\text{model}_i} - I_{\text{obs}_i})^2}{\sigma_{\text{obs}_i}^2}, \quad (11)$$

where I_{obs} are the four observed OH lines' intensities, I_{model} are the model line generated by RADEX, σ_{obs}^2 are the RMS of the four observed OH lines.

We varied T_k , OPR and N_{OH} to obtain the best fit to the observation at position 1, shown in Fig. 7. The best fitting T_k , OPR and N_{OH} are 31 K, 0.2 and $3.7 \times 10^{14} \text{ cm}^{-2}$, respectively. We also calculated the column density of OH at position 1 (assuming it to be optical thin and with no background emission) from the integrated intensity (in K km s^{-1}) of the 1667 MHz line through (e.g. Knapp & Kerr 1973; Turner & Heiles 1971)

$$\frac{N_{\text{OH}}}{\text{cm}^{-2}} = 2.22 \times 10^{14} \frac{\int T_b(V) dV}{\text{K km s}^{-1}}. \quad (12)$$

With these assumptions, N_{OH} is $0.5 \times 10^{14} \text{ cm}^{-2}$. When the excitation temperature of OH is so low that the background cannot be neglected, we have a correction factor f_{bg} (e.g. Harju et al. 2000; Suutarinen et al. 2011)

$$f_{\text{bg}} = \frac{1}{1 - T_{\text{bg}}/T_{\text{ex}}}. \quad (13)$$

When $T_{\text{bg}} \simeq 3.5 \text{ K}$ and $T_{\text{ex}} \simeq 4 \text{ K}$, $f_{\text{bg}} \simeq 8$, which yields $N_{\text{OH}} \simeq 4 \times 10^{14} \text{ cm}^{-2}$, almost the same as the fitted N_{OH} from RADEX (denoted $N_{\text{OH}}^{\text{RADEX}}$). The problem with using the ‘‘LTE method’’ is that we do not know the excitation temperature of OH. Instead, we have to assume an excitation temperature for OH, which has a major effect on the correction factor f_{bg} . Only with a statistical equilibrium calculation (e.g. RADEX) can we know the excitation temperature of OH exactly. We should be cautious about the low excitation temperature of OH, otherwise we may underestimate the column density of OH by a factor of 8 or more in many conditions where the LTE method is used.

Compared with $N_{\text{OH}}^{\text{RADEX}}$, the calculated N_{OH} through Eq. 12 and Eq. 13 (noted as $N_{\text{OH}}^{\text{LTE}}$ representing the ‘‘LTE method’’) is almost the same as $N_{\text{OH}}^{\text{RADEX}}$. The fitted opacity (Table 3) based on the model is relatively smaller ($\tau \sim 0.04\text{--}0.3$), which is consistent with the assumption of optical thin in the ‘‘LTE method’’.

Eq. 12 used to calculate N_{OH} assumes LTE, but the observed line ratio between OH 1665 MHz and 1667 MHz is obviously greater than 1, indicating that the OH at position 1 is far from LTE. The critical density of OH

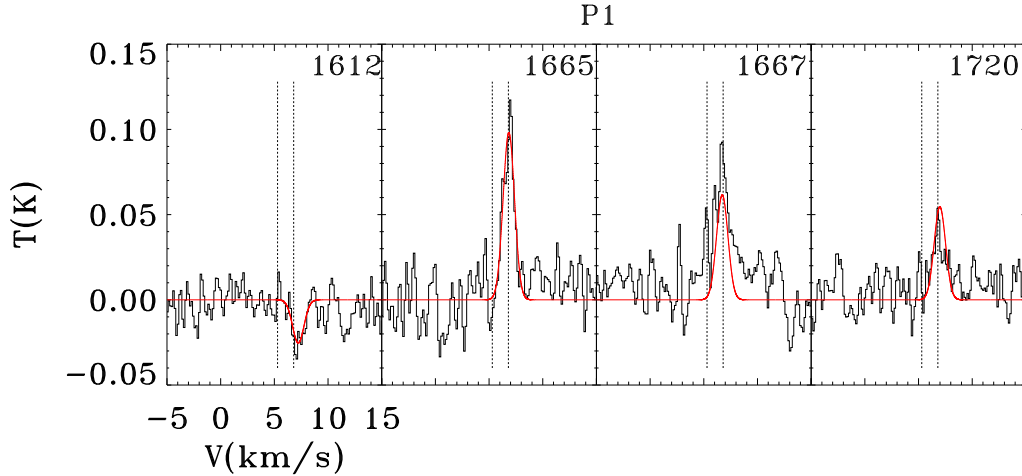


FIG. 7.— Observed OH lines(black lines) and the simulated OH profiles(red lines) using RADEX at position 1.

TABLE 3
OH PHYSICAL PARAMETERS AT POSITION 1

$n_{\text{H}_2}=62.6 \text{ cm}^{-3}$ $\text{OPR}=0.20$ $T_k = 31.0 \text{ K}$			
$N_{\text{OH}} = 3.7 \times 10^{14} \text{ cm}^{-2}$			
line	T_{ex} (K)	τ	T_A (K)
1612	3.1	0.045	-0.025
1665	4.1	0.163	0.098
1667	3.8	0.331	0.062
1720	5.4	0.024	0.055

HFS lines at 10-50 K is $1\text{--}20 \text{ cm}^{-3}$, indicating that OH excitation is dominated by collision in TBR with $n=70\text{--}600 \text{ cm}^{-3}$. Compared with OH, low-J ^{12}CO lines have a larger critical density about 2000 cm^{-3} . In most cases, when collision dominate the excitation, the LTE assumption is reasonable. Surprisingly, OH HFS lines are far from LTE, which has a low critical density. ^{12}CO is consistent with LTE as discussed in Section 3.2 with RADEX analysis. Considering for the complex energy level of OH, some pumping mechanism must be operative to yield the non-LTE of OH. We will have a detailed discussion in Section 5. A most possible mechanism is C-shock. The line ratio between 1665 MHz and 1667 MHz, and the integrated intensity of 1667 MHz across the boundary are listed in Table 4. In TBR-O, the line ratio is greater than 1. In TBR-I, the line ratio is between $\simeq 0.5$ and $\simeq 0.8$, within the range allowed by LTE.

The change of physical parameters across the boundary is partially listed in Table 5.

4.3. The Effect of the H_2 Ortho-to-Para Ratio (OPR) on Fitting

Owing to the different cross sections between OH and two spin symmetries of H_2 , i.e. ortho- H_2 and para- H_2 (Offer et al. 1994), the OPR plays a significant role in the excitation of OH. The exact value of OPR is important for producing the observed OH 1665/1667 intensity ratio in certain positions, such as for position 9, as shown in Fig. 8. Overall, the derived column density is insensitive to the numerical value of OPR, such as for position 10, as shown in Fig. 8. We will discuss this issue in a separate paper and focus on the dark gas and OH abundance content in the present work.

TABLE 4
OH PARAMETERS ALONG THE BOUNDARY

position	Ratio(1665/1667)	Intensity(1667) (K km s^{-1})
1	1.6 ± 0.18	0.21 ± 0.02
2	1.2 ± 0.14	0.20 ± 0.02
3	1.3 ± 0.13	0.22 ± 0.02
4	1.2 ± 0.12	0.24 ± 0.02
5	1.5 ± 0.14	0.29 ± 0.02
6	1.6 ± 0.13	0.26 ± 0.02
7	1.3 ± 0.10	0.35 ± 0.02
8	1.2 ± 0.08	0.31 ± 0.02
9	1.1 ± 0.05	0.42 ± 0.02
10	0.51 ± 0.02	0.49 ± 0.01
11	0.54 ± 0.02	0.53 ± 0.02
12	0.52 ± 0.02	0.50 ± 0.01
13	0.61 ± 0.02	0.49 ± 0.01
14	0.69 ± 0.02	0.48 ± 0.01
15	0.72 ± 0.02	0.42 ± 0.01
16	0.77 ± 0.03	0.40 ± 0.01
17	0.83 ± 0.04	0.37 ± 0.01

4.4. Physical Parameter Analysis

We define the CO-dark molecular gas fraction or dark gas fraction (DGF) as

$$\text{DGF} = 1 - \frac{N_{\text{CO}} \times 10^4}{N_{\text{H}_2}}, \quad (14)$$

which represents the fraction of H_2 that cannot be traced by CO emission. N_{CO} is obtained from the LTE calculation in Section 3.2 with the assumption that the abundance ratio of ^{12}CO to ^{13}CO is 65 (Langer & Penzias 1993; Liszt 2007). N_{H_2} is obtained from integration of the density profile in Section 4.1 along line of sight and the visual extinction is obtained from the relation $N(\text{H}_2)/A_V = 9.4 \times 10^{20} \text{ cm}^{-2} \text{ mag}^{-1}$, by assuming that the hydrogen is predominately in molecular form and standard grain properties are appropriate for the diffuse ISM (Orr et al. 2014). We averaged the column density of H_2 within the OH beam size ($\sim 3'$) at each position to make all the calculations refer to the same beam size. The variation of T_k , N_{OH} , $N_{\text{OH}}/N_{\text{H}_2}$ and DGF across the boundary as a function of extinction A_v is shown in Fig. 9. When the extinction A_v increases from 0.4 to 2.6

TABLE 5
THE CHANGE OF PHYSICAL PARAMETERS ACROSS THE BOUNDARY IN TAURUS

Position ID	Offset (')	Physical Parameters					
		T_k (K)		N_{OH} (10^{14} cm^{-2})		A_v (mag)	N_{OH}/N_{H_2} (10^{-7})
		$\mathcal{C}1$	$\mathcal{C}2$	$\mathcal{C}1$	$\mathcal{C}2$		
1 (outer)	-24.0	—	37	—	2.9	0.4	7.2^{+3}_{-2}
7 (I_{H_2} peak)	-6.0	25	35	2.9	1.3	1.3	$3.5^{+0.7}_{-0.3}$
9 (boundary)	0.0	26	32	1.5	4.9	1.8	$3.7^{+0.4}_{-0.2}$
11 (N_{H_2} peak)	6.0	10	27	1.5	4.5	2.4	$2.6^{+0.5}_{-0.3}$
12 (N_{CO} peak)	9.0	23	26	2.1	2.5	2.6	$1.9^{+0.4}_{-0.2}$
17 (inner)	24.0	24	—	3.3	—	1.5	$2.3^{+0.5}_{-0.3}$
							$0.75^{+0.1}_{-0.1}$

¹ DGF means dark gas fraction.

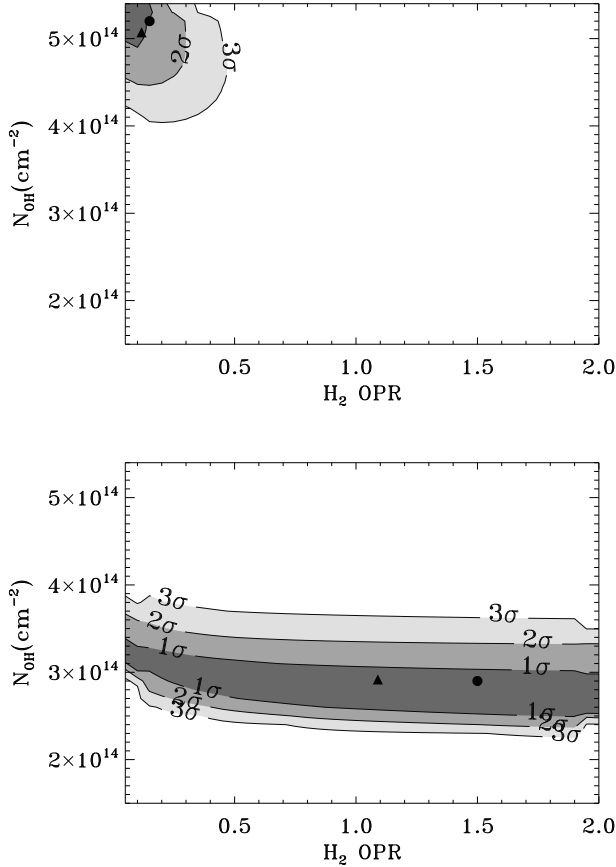


FIG. 8.— The probability space of each parameter at position 9 (top panel) and position 12 (bottom panel). In the contour map of probability space of two different parameters, different shades represent different confidence levels. The dot represents the χ^2_{min} fitted parameter, and the triangle represents the mean value of the parameter by integrating the parameter in probability space.

magnitudes, the kinetic temperature, the abundance of OH and the dark gas fraction all decrease. Especially, the DGF decreases from 80% to 20%, which means the amount of molecular gas that cannot be traced by CO is three times larger than that of molecular gas traced by CO when the extinction is below 1.4 magnitude. Empirically, CO intensities have been used as an indicator of the total molecular mass in the Milky way and in galaxies through the so-called “X-factor” with numerous well-

known caveats. In other words, we may seriously underestimate the amount of molecular gas through “X-factor” in low extinction clouds or regions of galaxies.

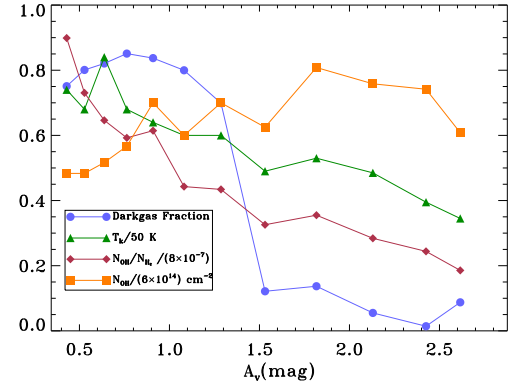


FIG. 9.— The change of T_k , N_{OH} , N_{OH}/N_{H_2} and DGF across the boundary as a function of the extinction A_v .

We parametrize the trend of N_{OH}/N_{H_2} and DGF in an exponential law and a gaussian profile, respectively, as shown in Fig. 10. The trend of N_{OH}/N_{H_2} can be fitted as

$$\frac{N_{OH}}{N_{H_2}} = 1.5 \times 10^{-7} + 0.9 \times 10^{-7} \times \exp\left(-\frac{A_v}{0.81}\right). \quad (15)$$

When the visual extinction is much larger than 0.48 mag, N_{OH}/N_{H_2} remains roughly a constant 1.5×10^{-7} . This constant indicates the abundance of OH at large visual extinctions within molecular clouds. A calculation using the Meudon PDR Code (Le Petit et al. 2006) with conditions appropriate for the TBR yields reasonably good agreement with OH abundance $[OH]/[H_2]$ for moderate extinction ($A_v \sim 2$). The prediction of $[OH]/[H_2]$ at extinctions at or below 1 mag is far lower (by a factor of 80) that we derive, suggesting that there may be an additional channel of OH production active, possibly due to the shock (e.g. Draine & Katz 1986) produced by the colliding streams. When shock waves propagate through the molecular ISM the ambient gas is compressed, heated, and accelerated. When temperature is above 300 K, the neutral-neutral reactions become important, which yield the overabundance of OH (Neufeld et al. 2002).

The trend of DGF can be fitted as,

$$\text{DGF} = 0.90 \times \exp\left[-\left(\frac{A_v - 0.79}{0.71}\right)^2\right]. \quad (16)$$

The peak of DGF is located at $A_v = 0.79$ mag, and the FWHM is 1.4 mag. When $0.79 < A_v < 2.5$ mag, the DGF decreases sharply with increasing A_v . This behavior of the DGF is expected theoretically, e.g. Planck and Fermi Collaborations (2015) found that CO-dark molecular dominates the molecular columns at $A_v \leq 1.5$ mag and Paradis et al. (2012) found an obvious deviation of the amount of gas traced by H I and ^{12}CO from that of the extinction data in the extinction range between 0.3 and 2 mag, while neither the low extinction (≤ 0.3 mag) nor the high extinction (≥ 2 mag) showing significantly deviation. In regions with sufficiently low visual extinction, H_2 cannot survive due to the destruction by UV photons. On the other hand, when the visual extinction is high enough, ^{12}CO can be formed and survive. At this point, the molecular gas can be well traced by ^{12}CO , so the DGF also drops at high visual extinction. When the visual extinction is between 0.4 and 1.3 mag, the abundance of H_2 is already a layer fraction of the total hydrogen abundance but ^{12}CO has not formed completely, so the DGF peaks under these conditions.

It is important to emphasize that the parameterized trends above can only be applied to the molecular gas with visual extinction between 0.4 and 1.3 mag, for which we have OH data and have modeled the lines successfully.

5. CONJUGATE EMISSION OF OH

As shown in Fig. 2, OH 1612 MHz lines appear to be absorption lines and OH 1720 MHz lines appear to be emission lines outside the boundary. However, it is quite different inside the boundary. OH 1612 MHz lines appear to be emission lines and OH 1720 MHz lines appear to be absorption lines inside the boundary. This inversion of satellite lines is known as conjugate emission of OH.

The mechanism for producing conjugate emission is asymmetry in pumping due to quantum selection rules in the OH rotational transition ladder, shown in Fig. 11. The 18 cm OH maser lines result from hyperfine transitions in the $^2\Pi_{3/2}(J = 3/2)$ level, which is the ground state. The 1720 MHz line is produced by a transition from a $F = 2$ to $F = 1$ state, while the 1612 MHz line is a transition from $F = 1$ to $F = 2$. Transitions between rotational levels are permitted when $|\Delta F| = 0, 1$. The $^2\Pi_{3/2}(J = 5/2)$ - $^2\Pi_{3/2}(J = 3/2)$ intra-ladder transition at $\lambda = 119 \mu\text{m}$ has hyperfine levels with $F = 2, 3$, and thus will preferentially populate the $F = 2$ levels in the ground state. The result is 1720 MHz inversion, and anti-inversion of the 1612 MHz line. A radiative transition from $^2\Pi_{1/2}(J = 1/2)$ - $^2\Pi_{3/2}(J = 3/2)$ cross-ladder transition at $\lambda = 79 \mu\text{m}$, which has hyperfine levels with $F = 0, 1$, will overpopulate the $F = 1$ levels in the OH ground state, producing 1612 MHz inversion and 1720 MHz anti-inversion.

For either of these pumping mechanisms, the FIR transition must be optically thick. When both FIR lines are optically thick, the 1612 MHz inversion dominates (Elitzur 1992). To produce 1720 MHz inversion and conjugate 1612 MHz absorption requires the $^2\Pi_{3/2}(J = 5/2)$ - $^2\Pi_{3/2}(J = 3/2)$ transition to be optically thick and the

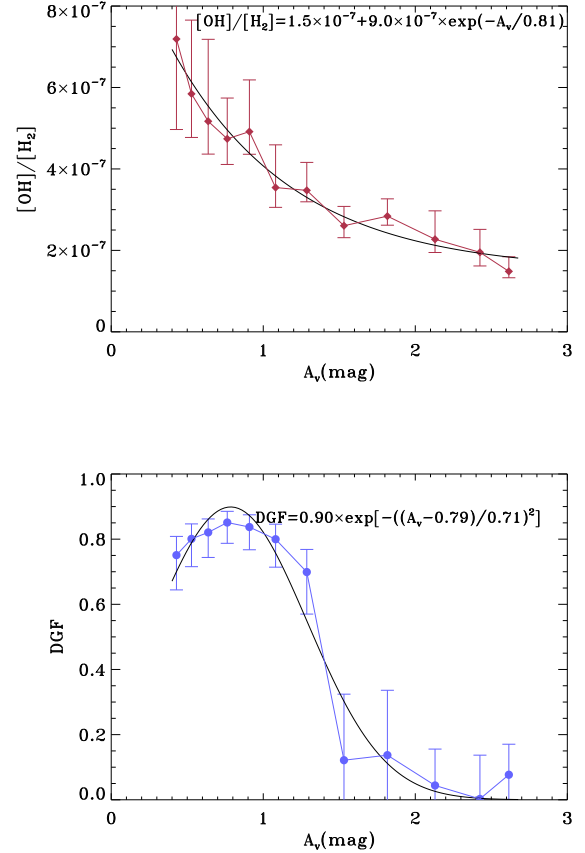


FIG. 10.— Parameterization of the change of $N_{\text{OH}}/N_{\text{H}_2}$ and DGF across the boundary as a function of extinction A_v . In the bottom panel of DGF plot, the value of DGF becomes slightly negative when $A_v \geq 1.8$ mag (the last three points) owing to there being slightly more H_2 traced by CO than that calculated from extinction. As the error in A_v increases at high extinction (by almost 50%, as shown in Fig. 2 in Orr et al. (2014)), we rescale N_{H_2} when $A_v \geq 1.8$ mag (the last three points) to be close to zero by the same factor of 1.6 in the bottom panel to ensure that $\text{DGF} \geq 0$.

$^2\Pi_{1/2}(J = 1/2)$ - $^2\Pi_{3/2}(J = 3/2)$ transition to be optically thin. The result is that for a column density per velocity interval just below $10^{15} \text{ cm}^{-2} \text{ km}^{-1}$ s, the 1720 MHz line is inverted and the 1612 MHz line is anti-inverted. The reverse behavior occurs for column density just above $10^{15} \text{ cm}^{-2} \text{ km}^{-1}$ s (van Langevelde et al. 1995).

The fitted column densities N_{OH} in Section 4.2 are all below $5.2 \times 10^{14} \text{ cm}^{-2}$, and the line widths at all positions are greater than 1 km s^{-1} . Thus the observed physical condition do not correspond to the reverse condition mentioned above. RADEX can not reproduce the OH 1720 MHz absorption when fitting OH lines inside the boundary, as shown in Fig. 12. There must be other pumping mechanisms, such as FIR emission from dust grains (Sivagnanam 2004), chemical pumping (Elitzur 1992), shocks (Pihlström et al. 2008), and/or a combination of these factors to invert the satellite lines of OH. RADEX takes into account none of the above. Given the lack of protostars or H II regions in the whole Taurus neighborhood and the possible existence of colliding streams seen in our data, we propose low velocity shocks

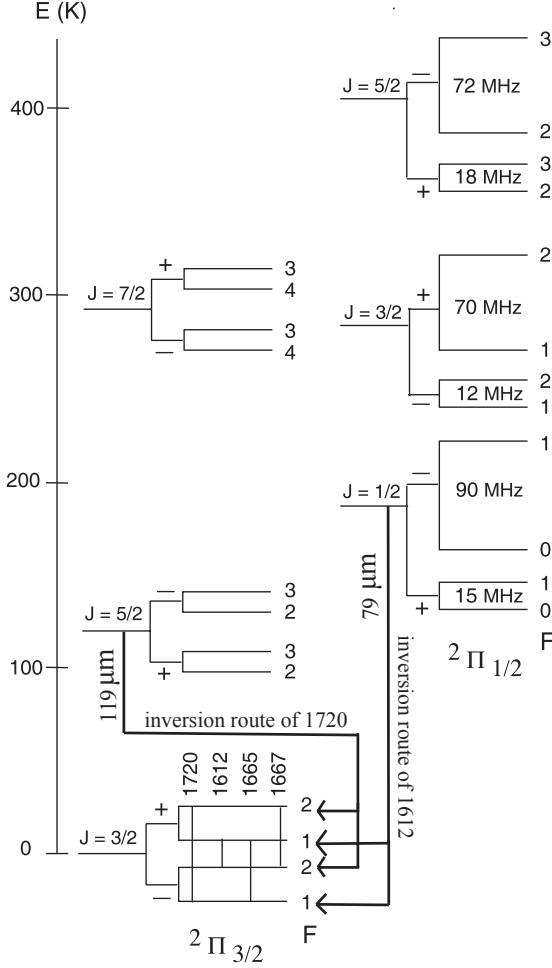


FIG. 11.— Rotational energy levels of OH, based on Lockett & Elitzur (2008). There are four transitions within each rotational level as a result of Λ -doubling and hyperfine splitting (not shown to scale).

as the main reason for the inversion of OH satellite lines.

6. SUMMARY AND CONCLUSIONS

We have mapped a sharp boundary region of the Taurus molecular cloud in the four ground-state transitions of the hydroxyl (OH) radical with the Arecibo telescope. We then carried out a combined analysis of our OH data along with H_r, ¹²CO J=1-0, ¹³CO J=1-0, with the non-LTE spectral analysis radiative transfer model, RADEX. Our main findings are the following:

1. The two main lines are seen in emission in all the positions across the boundary region. However the characteristics of the two satellite lines show significant differences across the boundary region. The satellite lines at 1612 and 1720 MHz show absorption and emission respectively outside the boundary, and show emission and absorption respectively inside the boundary.
2. Our cut perpendicular to the boundary shows that OH has two kinematic components and one component shifts from 5.3 km s⁻¹ to 6 km s⁻¹, which seems

to indicate colliding streams or gas flow at the boundary region.

3. We have used a cylindrical model and RADEX to fit the OH lines to determine the physical parameters, including T_k , the OPR, N_{OH} , across the boundary. All the physical parameters can be well constrained. The excitation of OH is far from LTE.
4. We have derived the OH abundance (N_{OH}/N_{H_2}) profile across the boundary. N_{OH}/N_{H_2} decreases from 8×10^{-7} to 1×10^{-7} as A_v increases from 0.4 to 2.7 mag, following an exponential law $[OH]/[H_2] = 1.5 \times 10^{-7} + 9.0 \times 10^{-7} \times \exp(-A_v/0.81)$. OH abundance $[OH]/[H_2]$ for moderate extinction ($A_v \sim 2$) is consistent with that of PDR model. But OH at extinctions at or below 1 mag is overabundant than the prediction of PDR model by a factor of 80. The overabundance of OH is likely the result of a C-shock, which accelerates the neutral-neutral reactions.
5. We obtained the fraction of CO-dark molecular gas (DGF) across the boundary. The DGF decreases from 0.8 to 0.2 following a gaussian profile $DGF = 0.90 \times \exp(-(\frac{A_v - 0.79}{0.71})^2)$. This trend of DGF is expected from theory. The DGF drops at low visual extinction due to the reduced abundance of H₂, and drops at high visual extinction due to the complete conversion of carbon to CO. The DGF is thus maximum in the range where H₂ has already formed but ¹²CO has not formed completely. This is of significance in estimating the amount of molecular gas in low extinction clouds or regions of galaxies with similar condition.
6. We detected the conjugate emission of OH 1612 MHz and 1720 MHz components. The complementary switching between emission and absorption of 1612 MHz and 1720 MHz, respectively, suggests that an incompletely modeled pumping mechanism must be operative, the most likely of which is C-shock.

This work is partly supported by the China Ministry of Science and Technology under State Key Development Program for Basic Research (973 program) No. 2012CB821802, the National Natural Science Foundation of China No. 11373038, No. 11373045, and the Strategic Priority Research Program "The Emergence of Cosmological Structures" of the Chinese Academy of Sciences, Grant No. XDB09010302. This work was carried out in part at the Jet Propulsion Laboratory, which is operated for NASA by the California Institute of Technology. Di Li acknowledges support from the Guizhou Scientific Collaboration Program (#20130421). We are grateful to Carl Heiles and Z.Y. Ren for their kind and valuable advice and support. We would like to thank the anonymous referee for the careful inspection of the manuscript and constructive comments particularly the important suggestions to add the comparison with PDR model for similar G_0 and n_H values to improve the quality of this study.

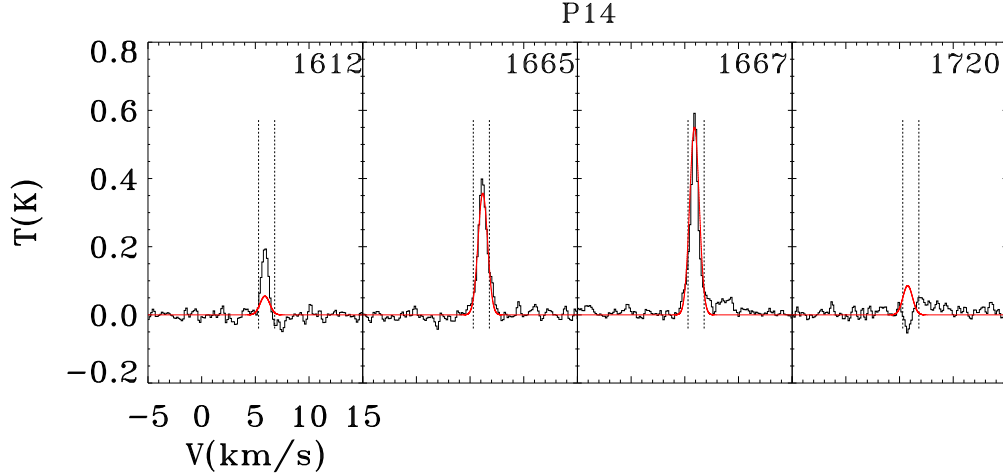


FIG. 12.— The panel shows the observed OH lines (black lines) and the simulated OH profiles (red lines) with RADEX at position 14.

REFERENCES

- Anderl, S., Guillet, V., Pineau des Forêts, G., & Flower, D. R. 2013, *A&A*, 556, AA69
- Draine, B. T., & Katz, N. 1986, *ApJ*, 306, 655
- Draine, B. T., & Katz, N. 1986, *ApJ*, 310, 392
- Elitzur, M. 1992, *Astronomical Masers*, Vol. 170 (Dordrecht: Kluwer)
- Flagey, N., Noriega-Crespo, A., Boulanger, F., et al. 2009, *ApJ*, 701, 1450
- Goldsmith, P. F., Heyer, M., Narayanan, G., et al. 2008, *ApJ*, 680, 428
- Goldsmith, P. F., Velusamy, T., Li, D., & Langer, W. D. 2010, *ApJ*, 715, 1370
- Harju, J., Winnberg, A., & Wouterloot, J. G. A. 2000, *A&A*, 353, 1065
- King, I. 1962, *AJ*, 67, 471
- Knapp, G. R. & Kerr, F. J. 1973, *AJ*, 78, 453
- Langer, W. D., & Penzias, A. A. 1993, *ApJ*, 408, 539
- Larson, R. B. 1981, *MNRAS*, 194, 809
- Le Petit, F., Nehmé, C., Le Bourlot, J., & Roueff, E. 2006, *ApJS*, 164, 506
- Li, D. 2002, PhD thesis, Cornell University
- Li, D., Xu, D., Heiles, C., Pan, Z., & Tang, N. 2015, *PKAS*, 30, 75
- Liszt, H. S. 2007, *A&A*, 476, 291
- Lockett, P., & Elitzur, M. 2008, *ApJ*, 677, 985
- Medling, A. M., U, V., Rich, J. A., et al. 2015, *MNRAS*, 448, 2301
- Narayanan, G., Heyer, M. H., Brunt, C., et al. 2008, *ApJS*, 177, 341
- Neufeld, D. A., Kaufman, M. J., Goldsmith, P. F., Hollenbach, D. J., & Plume, R. 2002, *ApJ*, 580, 278
- Offer, A. R., van Hemert, M. C., & van Dishoeck, E. F. 1994, *J. Chem. Phys.*, 100, 362
- Orr, M. E., Pineda, J. L., & Goldsmith, P. F. 2014, *ApJ*, 795, 26
- Padoan, P., Cambrésy, L., & Langer, W. 2002, *ApJ*, 580, L57
- Park, Y.-S., & Hong, S. S. 1995, *A&A*, 300, 890
- Paradis, D., Dobashi, K., Shimoikura, T., et al. 2012, *A&A*, 543, A103
- Peek, J. E. G., Heiles, C., Douglas, K. A., et al. 2011, *ApJS*, 194, 20
- Pihlström, Y. M., Fish, V. L., Sjouwerman, L. O., et al. 2008, *ApJ*, 676, 371
- Pineda, J. L., Goldsmith, P. F., Chapman, N., et al. 2010, *ApJ*, 721, 686
- Planck & Fermi Collaborations 2015, *A&A*, 582, A31
- Sivagnanam, P. 2004, *MNRAS*, 347, 1084
- Suutarinen, A., Geppert, W. D., Harju, J., et al. 2011, *A&A*, 531, A121
- Tennyson, J. (ed.) 2005, *Astronomical spectroscopy: An Introduction to the Atomic and Molecular Physics of Astronomical Spectra* (London: Imperial College Press)
- Tielens, A. G. G. M. 2005, *The Physics and Chemistry of the Interstellar Medium*, (UK: Cambridge University Press)
- Timmermann, R. 1998, *ApJ*, 498, 246
- Turner, B. E. & Heiles, C. 1971, *ApJ*, 170, 453
- van der Tak, F. F. S., Black, J. H., Schöier, F. L., Jansen, D. J., & van Dishoeck, E. F. 2007, *A&A*, 468, 627
- van Langevelde, H. J., van Dishoeck, E. F., Sevenster, M. N., & Israel, F. P. 1995, *ApJ*, 448, L123
- Winnberg, A., Grasshoff, M., Goss, W. M., & Sancisi, R. 1980, *A&A*, 90, 176